

Atomistic Simulation of Realistically Sized Nanodevices Using NEMO 3-D: Part II – Applications

Gerhard Klimeck^{1,2}, Shaikh Ahmed¹, Neerav Kharche¹, Marek Korkusinski³, Muhammad Usman¹, Marta Prada¹, and Timothy B. Boykin⁴

Abstract—In Part-I, development and deployment of a general Nanoelectronic Modeling tool (NEMO 3-D) has been discussed. Based on the atomistic valence-force field (VFF) and the $sp^3d^s^*$ nearest-neighbor tight-binding models, NEMO 3-D enables the computation of strain and electronic structure in nanostructures consisting of over 64 and 52 million atoms, corresponding to volumes of $(110\text{nm})^3$ and $(101\text{nm})^3$, respectively. In this part, successful applications of NEMO 3-D are demonstrated in the atomistic calculation of single-particle electronic states of realistically-sized (1) self-assembled quantum dots (QDs) including long-range strain and piezoelectricity, (2) stacked quantum dot system as used in quantum cascade lasers, (3) SiGe quantum wells (QWs) for quantum computation, and (4) SiGe nanowires. These examples demonstrate the broad NEMO 3-D capabilities and indicate the necessity of multimillion atomistic electronic structure modeling.

Index Terms—Atomistic simulation, NEMO 3-D, Nanostructures, Strain, Piezoelectricity, Valley splitting, Quantum computation, Tight binding, Keating model, Quantum dot, Quantum well, Nanowire.

I. INTRODUCTION

THIS article describes NEMO 3-D capabilities in the simulation of 3 (three) different classes of nanodevices of carrier confinement in 3, 2, and 1 dimensions in the GaAs/InAs and SiGe materials systems.

Single and Stacked Quantum Dots (confinement in 3 dimensions). Quantum dots (QDs) are solid-state semiconducting nanostructures that provide confinement of charge carriers (electrons, holes, excitons) in all three spatial dimensions resulting in strongly localized wave functions, discrete energy eigenvalues and subsequent interesting physical and novel device properties [1][2][3][4][5]. Existing nanofabrication techniques tailor QDs in a variety of types, shapes and sizes. Within bottom-up approaches, QDs can be realized by colloidal synthesis at benchtop conditions.

Quantum dots thus created have dimensions ranging from 2–10 nanometers corresponding to 100–100,000 atoms. On the other hand, self-assembled quantum dots (SAQDs), in the coherent Stranski-Krastanov heteroepitaxial growth mode, nucleate spontaneously within a lattice mismatched material system (for example, InAs grown on GaAs substrate) under the influence of strain in certain physical conditions during molecular beam epitaxy (MBE) and metalorganic vapor phase epitaxy (MOVPE) [1][6]. The strain produces coherently strained quantum-sized islands on top of a two-dimensional wetting-layer. The islands can be subsequently buried to form the quantum dot. Semiconducting QDs grown by self-assembly are of particular importance in quantum optics [7][8], since they can be used as detectors of infrared radiation, optical memories, and in laser applications. The delta-function-like energy dependence of density of states and the strong overlap of spatially confined electron and hole wavefunctions provide ultra-low threshold current densities, high temperature stability of the threshold current and high material and differential quantum gain/yield. Strong oscillator strength and non-linearity in the optical properties have also been observed [1][8]. Self-assembled quantum dots also have potential for applications in quantum cryptography as single photon sources and quantum computation [9][10]. In electronic applications QDs have been used to operate like a single-electron transistor and demonstrate pronounced Coulomb blockade effect. Self-assembled QDs, with an average height of 1–5 nm, are typically of size (base length/diameter) 5–50 nm and consist of 5,000–2,000,000 atoms. Arrays of quantum-mechanically coupled (stacked) self-assembled quantum dots can be used as optically active regions in high-efficiency, room-temperature lasers. Typical QD stacks consist of 3–7 QDs with typical lateral extension of 10–50 nm and dot height of 1–3 nm. Such dots contain 5–50 million atoms in total, where atomistic details of interfaces are indeed important [11].

Quantum Wires (confinement in 2 dimensions). For quite some time, nanowires have been considered a promising candidate for future building block in computers and information processing machines [12][13][14][15][16]. Nanowires are fabricated from different materials (metal, semiconductor, insulator and molecular) and assume different cross-sectional shapes, dimensions and diameters. Electrical conductivity of nanowires is greatly influenced by edge effects

¹School of Electrical and Computer Engineering and Network for Computational Nanotechnology, Purdue University, West Lafayette, IN 47907, USA. Tel: (765) 494 9212, Fax: (765) 494 6441, E-mail: gekco@purdue.edu

²Jet Propulsion Laboratory, California Institute of Technology, Pasadena, CA 91109.

³Institute for Microstructural Sciences, National Research Council of Canada, 1200 Montreal Road, Ottawa, Ontario K1A 0R6.

⁴Electrical and Computer Engineering Dept., The University of Alabama in Huntsville, Huntsville, AL 35899.

on the surface of the nanowire and is determined by quantum mechanical conductance quanta. In the nanometer regime, the impact of surface roughness or alloy disorder on electronic bandstructure need be atomistically studied to further gauge the transport properties of nanowires.

Quantum Wells (confinement in 1 dimension). QW devices are already a de-facto standard technology in MOS devices and QW lasers. They continue to be examined carefully for ultra-scaled devices where interfacial details turn out to be critical. Composite channel materials with GaAs, InAs, InSb, GaSb, and Si are being considered [17][18], which effectively constitute QWs. Si QWs buffered/strained by SiGe are considered for Quantum Computing (QC) devices where valley-splitting (VS) is an important issue [19]. Si is desirable for QC due to its long spin-decoherence times, scaling potential and integrability within the present microelectronic infrastructure. In strained Si 6-fold valley-degeneracy of Si is broken into lower 2-fold and raised 4-fold valley-degeneracies. The presence of 2-fold valley-degeneracy is a potential source of decoherence which leads to leakage of quantum information outside qubit Hilbert space. Therefore, it is of great interest to study the lifting of remaining 2-fold valley degeneracy in strained Si due to sharp confinement potentials in recently proposed [19] SiGe/Si/SiGe quantum well (QW) heterostructures based quantum computing architectures.

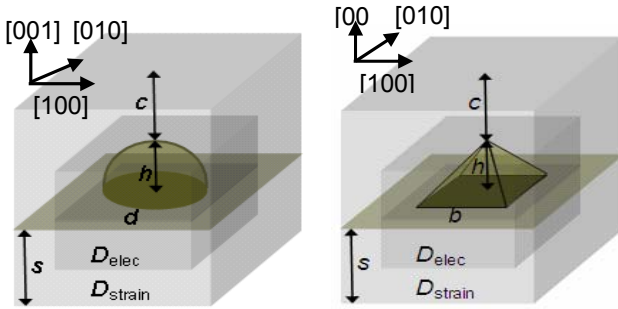


Fig. 1. Simulated InAs/GaAs quantum dots with dome and pyramidal shape. Two simulation domains are shown. D_{elec} : central domain for electronic structure calculation, and D_{strain} : larger/outer domain for strain calculation. In the figure: s is the substrate height, c is the cap layer thickness, h is the dot height, d is the dot diameter and b is the dot base length.

II. SIMULATION RESULTS

(A) Strain and Piezoelectricity in InAs/GaAs Single QDs

The dome and pyramid shaped InAs QDs that are studied first in this work are embedded in a GaAs barrier material (schematic shown in Figure 1) and have diameter (base length) and height of 11.3 nm and 5.65 nm respectively, and are positioned on a 0.6-nm-thick wetting layer [20][21]. The simulation of strain is carried out in the larger computational box (width D_{strain} and height H), while the electronic structure computation is usually restricted to the smaller domain (width D_{elec} and height H_{elec}). All the strain simulations in this

category fix the atom positions on the bottom plane to the GaAs lattice constant, assume periodic boundary conditions in the lateral dimensions, and open boundary conditions on the top surface. The inner electronic box assumes closed boundary conditions with passivated dangling bonds [22]. The strain domain contains ~ 3 M atoms while the electronic structure domain contains ~ 0.3 M atoms.

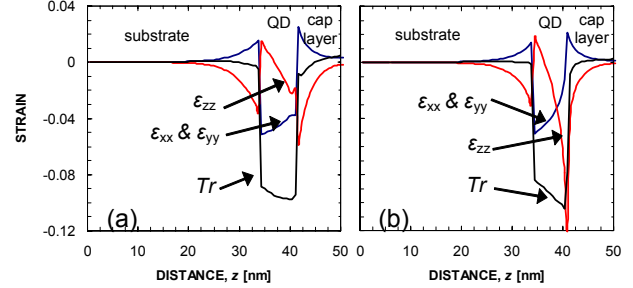


Fig. 2. Atomistic *diagonal* strain profile along the [001], z direction. (a) Dome shaped dot with Diameter, $d = 11.3$ nm and Height, $h = 5.65$ nm. (b) Pyramidal dot with Base, $b = 11.3$ nm and Height, $h = 5.65$ nm. Strain is seen to penetrate deep inside the substrate and the cap layer. Also, noticeable is the gradient in the trace of the hydrostatic strain curve (Tr) inside the dot region that results in optical polarization anisotropy and non-degeneracy in the electronic conduction band P . Atomistic strain thus lowers the symmetry of the quantum dot.

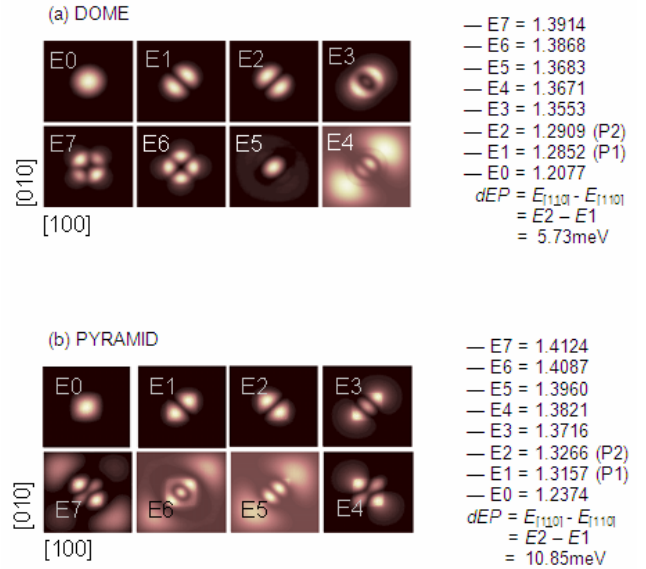


Fig. 3. Conduction band wavefunctions and spectra (eV) for first eight energy levels in the (a) Dome shape and (b) Pyramidal quantum dot structures. Atomistic strain is included in the calculation. Note the optical anisotropy and non-degeneracy in the P energy level. The first state is oriented along [110] direction and the second state along $[1\bar{1}0]$ direction.

Impact of strain. Strain modifies the effective confinement volume in the device, distorts the atom bonds in length and angles, and hence modulates the local Bandstructure and the confined states. Figure 2 show the diagonal (biaxial)

components of strain distribution along the [001] direction in both the quantum dots (cut through the center of the dot). There are two salient features in both these plots: (a) The atomistic strain is long-ranged and penetrates deep into both the substrate and the cap layers, and (b) all the components of biaxial stress has a non-zero slope inside the quantum dot region. The presence of the gradient in the trace of the hydrostatic strain introduces unequal stress in the zincblende lattice structure along the depth, breaks the equivalence of the [110] and $[1\bar{1}0]$ directions, and finally breaks the degeneracy of the first excited electronic state (the so called P level). Figure 3 shows the wavefunction distribution for the first 8 (eight) conduction band electronic states within the device

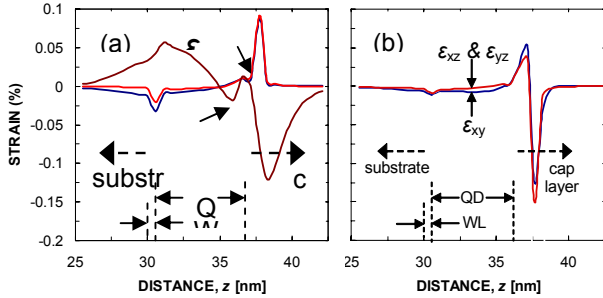


Fig. 4. Atomistic *off-diagonal* strain profile along the z (vertical) direction which in effect induces polarization in the quantum dot structure. (a) Dome shape dot with Diameter, $d = 11.3$ nm and Height, $h = 5.65$ nm. (b) Pyramidal dot with Base, $b = 11.3$ nm and Height, $h = 5.65$ nm.

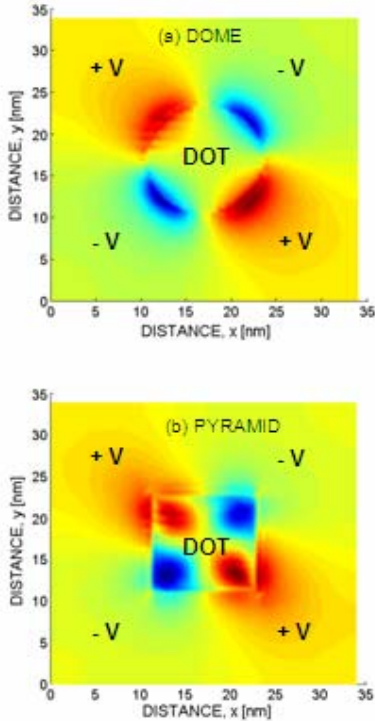


Fig. 5. Potential surface plot of (a) dome shape (b) pyramidal quantum dot in the XY plane at $z = 1$ nm from the base of the dot.

region for both the dots (in a 2-D projection). Note the optical anisotropy and non-degeneracy in the first excited (P) energy level. The first P state is oriented along the [110] direction and the second P state along the $[1\bar{1}0]$ direction. The individual energy spectrum is also depicted in this figure which reveals the value of the P level splitting/non-degeneracy (defined as $E_{1\bar{1}0} - E_{110}$) to be about 5.73 meV and 10.85 meV for the dome shaped and pyramidal quantum dots, respectively. Although both the two dots have the same qualitative trend in diagonal strain profiles and similar wavefunction distribution, the reason for a larger split and hence pronounced anisotropy of P level in the pyramidal quantum dot is due to the presence of larger gradient of the hydrostatic strain, as can be seen in Figure 2, inside the dot region. In other words, as far as crystal symmetry lowering is concerned, atomistic strain has stronger impact in the pyramidal dot than it has in the dome shaped dot.

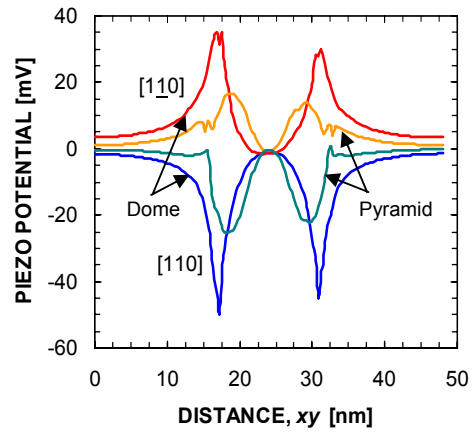


Fig. 6. Potential along [110] and $[1\bar{1}0]$ directions at $z = 1$ nm from the base of the dot. Notice the induced polarization in the potential profile and the unequal values of potential along the [110] and $[1\bar{1}0]$ directions. Also, dome shape dot induces stronger potential ($d/b = 11.3$ nm and $h = 5.65$ nm).

Impact of piezoelectric field. The presence of non-zero off-diagonal strain tensor elements leads to the generation of a piezoelectric field in the quantum dot structure, which is incorporated in the simulations as an external potential by solving the Poisson equation on the zincblende lattice. Figure 4 shows the atomistic off-diagonal strain profiles in both the quantum dots with heights, h of 5.65 nm and diameter (base length) of 11.3 nm. The off-diagonal strain tensors are found to be larger in the dome shaped dot. The off-diagonal strain tensors are used to calculate the first-order polarization in the underlying crystal (please see Ref. [20] for the governing equations) which gives rise to a piezoelectric charge distribution throughout the device region and then used to calculate the potential by solving the Poisson equation. The relevant parameters for the piezoelectric calculation are taken from Ref. [20]. Experimentally measured polarization constants of GaAs and InAs materials (on unstrained bulk) values of -0.16 C/m² and -0.045 C/m² are used. The second

order piezoelectric effect [23] is neglected here because of unavailability of reliable relevant polarization constants for an InAs/GaAs quantum dot structures.

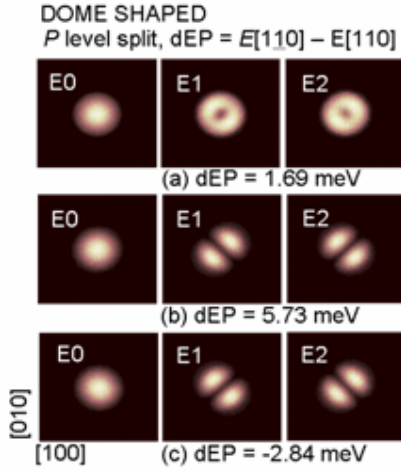


Fig. 7. Conduction band wavefunctions for first three energy levels in the dome shaped quantum dot structure with diameter, $b = 11.3$ nm and height, $h = 5.65$ nm (a) without strain and piezoelectricity, $E_{[1\bar{1}0]} - E_{[110]} = 1.69$ meV (b) with atomistic strain, $E_{[1\bar{1}0]} - E_{[110]} = 5.73$ meV and (c) with strain and piezoelectricity, $E_{[1\bar{1}0]} - E_{[110]} = -2.84$ meV. Piezoelectricity *flips* the wavefunctions.

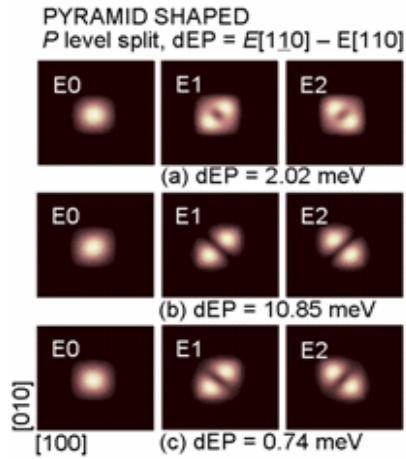


Fig. 8. Conduction band wavefunctions for first three energy levels in the pyramidal quantum dot structure with base, $b = 11.3$ nm and height, $h = 5.65$ nm (a) without strain and piezoelectricity, $E_{[1\bar{1}0]} - E_{[110]} = 2.02$ meV (b) with atomistic strain, $E_{[1\bar{1}0]} - E_{[110]} = 10.85$ meV and (c) with strain and piezoelectricity, $E_{[1\bar{1}0]} - E_{[110]} = 0.74$ meV. Piezoelectricity does *not* flip the wavefunctions.

The calculated piezoelectric potential contour plots in the XY plane are shown in Figure 5 revealing a pronounced polarization effect induced in the structure. It is found that in both the dots piezoelectric field alone favors the $[1\bar{1}0]$ orientation of the P level. Shown in Figure 6 is the asymmetry in potential profile due to *atomistic* strain and inequivalence in

the piezoelectric potential along $[110]$ and $[1\bar{1}0]$ directions at a certain height $z = 1$ nm from the base of the dots.

Figures 7 and 8 show the conduction band wavefunctions for the ground and first three excited energy states in the dome and pyramidal quantum dot structures with diameter (base length) of 11.3 nm and height, h of 5.65 nm, respectively. In Figures 7a and 8a strain and piezoelectricity are *not* included in the calculation. The weak anisotropy in the P level is due to the atomistic interface and material discontinuity. Material discontinuity mildly favors the $[110]$ direction in both the dots. In Figures 7b and 8b atomistic strain and relaxation is included resulting in a 5.73 meV (dome) and 10.85 meV (pyramidal) splits in the P energy levels. Strain favors the $[110]$ direction in both the dots. In Figures 7c and 8c piezoelectricity is included on top of strain inducing a split of -2.84 meV (dome) and 9.59 meV (pyramid) in the P energy level. There is a noticeable difference in Figures 7c and 8c. In the case of a dome shaped dot (Figure 7c), the first P state is oriented along $[1\bar{1}0]$ direction and the second state along $[110]$ direction; piezoelectricity thereby has not only introduced a global shift in the energy spectrum but also *flipped* the orientation of the P states. In the case of a pyramidal dot (Figure 8c) the energetic sequence of the P states remains unchanged. The underlying reason behind this difference in orientation polarization due to piezoelectricity can be explained by the unequal potential induced as depicted in the 1-D potential plot in Figure 6, which really is induced by the off-diagonal crystal distortion depicted in Figure 4. The pyramidal dot does not build-up as much off-diagonal strain due to the alignment of its facets with the crystal. As a result the piezoelectric fields are reduced.

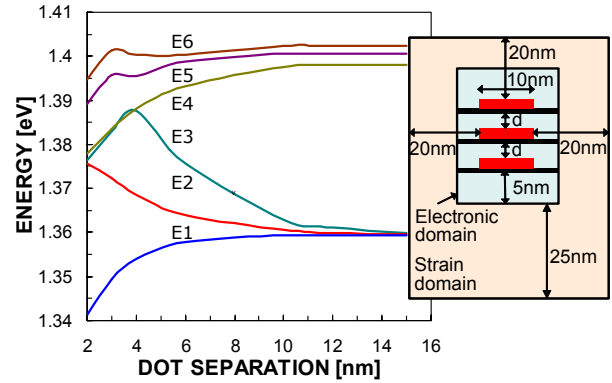


Fig. 9. Electron state energies in the quantum dot molecule as a function of interdot separation. The strain simulation domain contains 8–13 M atoms and the electronic structure domain contains 0.5–1.1M atoms.

(B) Stacked Quantum Dot System

Self-assembled quantum dots can be grown as stacks where the QD distance can be controlled with atomic layer control. This distance determines the interaction of the artificial atom states to form artificial molecules. The design of QD stacks becomes complicated since the structures are subject to inhomogeneous, long-range strain and growth imperfections

such as non-identical dots and inter-diffused interfaces. Quantum dot stacks consisting of three QD layers are simulated next (see inset of Figure 9). The InAs quantum dots are disk shaped with diameter 10 nm and height 1.5 nm positioned on a 0.6 nm thick wetting layer. The substrate thickness under the first wetting layer is kept constant at 30nm and the cap layer on top of the topmost dot is kept at 10 nm for all simulations. The strain simulation domain contains 8–13 M atoms and the electronic structure domain contains 0.5–1.1M atoms.

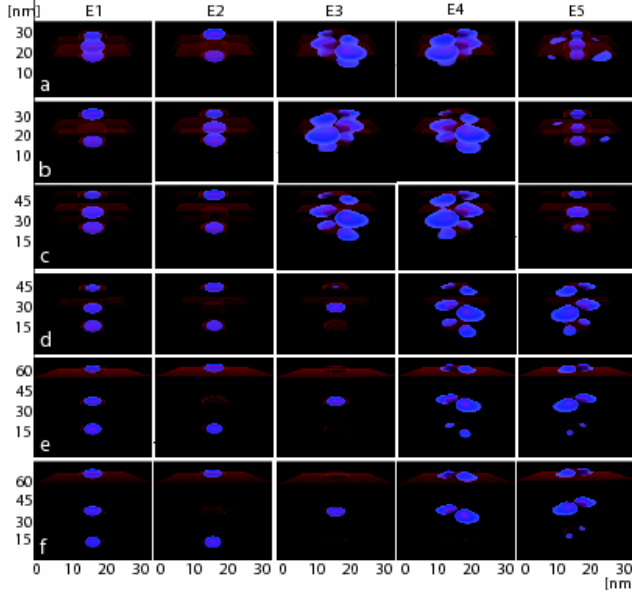


Fig. 10. First five electron states wavefunction magnitudes (columns) with QD 2, 3, 4, 6, 10 and 12 nm separation (rows).

Figure 9 shows the electron state energy as a function of inter-dot separation. In a system without inhomogeneous strain one would expect the identical dots to have degenerate eigenstate energies for large dot separations. Strain breaks the degeneracy even for large separations. The strain field clearly extends over the distance of 15 nm quantum dot separation (which is why they physically do not grow on top of each other). As the dot separation is narrowed the dots interact with each other mechanically through the strain field as well as quantum mechanically through wavefunction overlaps. The set of lowest states E0-2 clearly show the state repulsion of bonding and anti-bonding molecular states for short inter-dot distances. Figure 10 shows cross-sectional cuts in the growth direction and one lateral direction through the middle of the 3-D wavefunctions. The wavefunctions are quite clearly separated into the individual dots with little overlap across the dots for dot separations of 15 nm and 10 nm. For 2-6 nm separation, wavefunction overlap can be observed. The reduction of E2 energy with decreasing distance for 2-4 nm can be associated with a cross-over of p-symmetry states.

Whether or not the coupled dot system favors the top-most or bottom-most QD to peak the ground state wavefunction is a complicated interplay of strain, QD size, and wavefunction overlap. Only a detailed simulation can reveal that interplay.

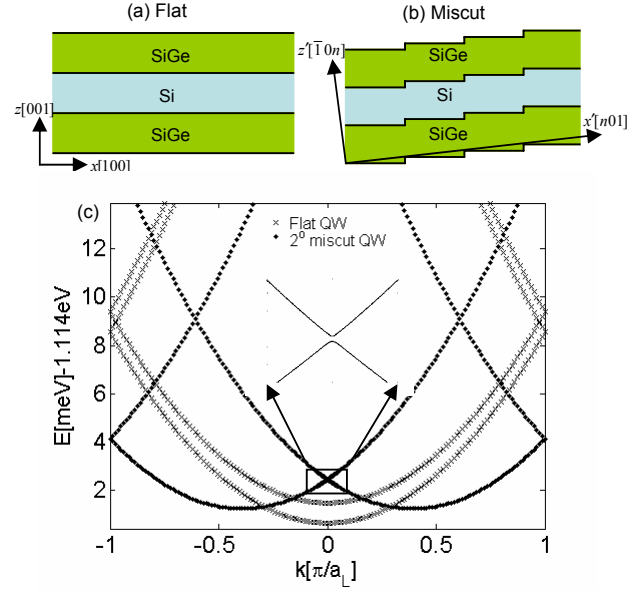


Fig. 11. (a) Schematic of a SiGe/Si/SiGe QW heterostructure grown on [001] substrate. The crystal symmetry directions are along x and z . (b) Schematic of a quantum well unit cell grown on $z'[\bar{1}0n]$ miscut substrate. The unit cell is periodic along $x'[\bar{n}01]$ and y' directions and confined in $z'[\bar{1}0n]$ direction. Miscut angle is $\theta_T = \tan^{-1}(1/n)$. The step height is one atomic layer ($a/4$), where a is lattice constant. (c) Band structure of 5.26 nm thick flat QW along x and 2^0 miscut QW along x' direction. Flat QW shows the presence of two non-degenerate valleys separated by an energy known as VS. Miscut QW shows the presence of two degenerate valleys centered at $\pm k_{x'}^0$. Interaction between these valleys at $\pm k_{x'} = 0$ causes a minigap (Δ_m) as shown in the inset. Lowest valleys are degenerate. Here, $a_L = na_{Si}$ and $n=28$ for 2^0 miscut. SiGe buffer layers are not included in electronic structure calculation domain for these plots.

(C) SiGe Quantum Well

Miscut (vicinal) surfaces (Figure 11b) as opposed to flat surfaces (Figure 11a) are often used to ensure uniform growth of Si/SiGe heterostructures. Miscut has a dramatic effect on bandstructure of Si QW. Bandstructure of a flat Si QW has two valleys centered at $\pm k_x = 0$ and separated by an energy known as valley-splitting (VS) [24][25]. VS in a flat QW is a result of interaction among states in bulk z -valleys centered at $k_z = k_m$, where k_m is position of the valley-minimum in strained Si. In a miscut QW lowest lying valleys are

degenerate with minima at $\pm k_x^0$. Valley-valley interaction at $\pm k_x = 0$ causes formation of a minigap (Δ_m). Thus atomic scale modulation of surface topology leads to very different electronic structures in flat and miscut QWs. As a consequence of this, flat and miscut QWs respond differently to the applied magnetic fields. In the presence of lateral confinement in miscut QW the two degenerate valleys in Figure 11c interact giving rise to VS.

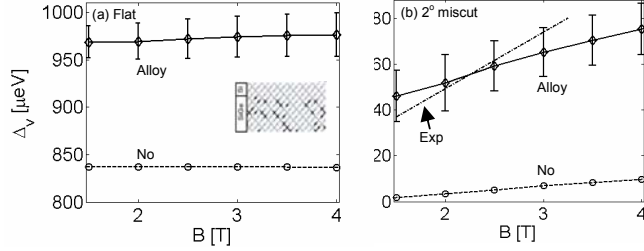


Fig. 12. (a) VS of the first Landau-level in a 10nm thick flat strained Si QW. VS increases due to the alloy-disorder (as shown in the inset) in SiGe buffer layers. (b) VS of the first Landau-level in a 2° miscut strained Si QW. Presence of miscut surfaces leads to significant suppression in VS. Inclusion of realistic alloy-disorder in SiGe buffer layers raise the VS to experimentally observed values. Error bars represent standard deviation in VS.

The VS is often measured using magnetic probe techniques such as Shubnikov de Haas oscillations or electron-valley resonance (EVR) [26]. In these measurements in plane confinement of the Landau-levels is provided by the magnetic field. Figure 12a and 12b show the dependence of VS on applied magnetic field in flat and 2° miscut QWs. In a flat QW VS is independent of magnetic field because in these QWs VS arises from z-confinement provided by the confining SiGe buffers. In miscut QWs, however, VS arises from the interaction of two degenerate valleys centered at $\pm k_x^0$ along x' direction. Therefore, x' confinement arising from the applied magnetic field results in the dependence of VS on magnetic field. At low magnetic fields this dependence is linear. SiGe alloy disorder shown in inset of Figure 12a is inherently present Si/SiGe heterostructures. In tight-binding calculations alloy-disorder translates into atom-disorder and inhomogeneous strain disorder.

Simulation Domain. Strain disorder is known to have long range nature (see for example the QD simulations in Figure 2). 40nm of SiGe layers are included on the top and the bottom of 10nm Si QW for strain calculations. This SiGe thickness is sufficient to model the long-range strain disorder, where the detailed strain boundary conditions are not important and the SiGe volume exceeds the Si QW volume significantly. SiGe buffers provide electronic confinement of approximately 100meV due to which the electronic states of interest in this problem are spatially confined to the QW and only weakly

penetrate into the SiGe buffer. Therefore one can safely reduce the electronic structure domain to 3nm of SiGe buffer around the Si QW. For this setup the strain calculation requires 3.6 M atoms and the electronic structure calculation requires 0.7M atoms. For the idealized geometries without a SiGe buffer, a homogeneous lattice distortion of $\epsilon_{||} = 0.013$ is assumed throughout the Si QW, as approximated from the full SiGe buffer system calculation and hard wall boundary conditions are assumed in z-direction. Such electronic structure calculations require $\sim 50,000$ atoms.

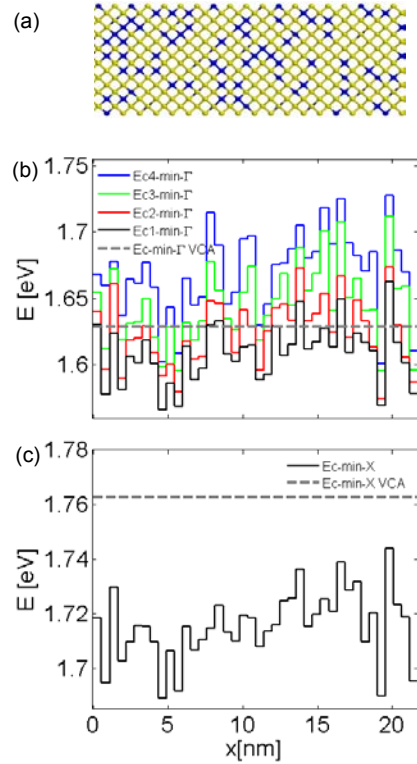


Fig. 13. (a) Atomistically resolved disorder in the $\text{Si}_{0.8}\text{Ge}_{0.2}$ $40 \times 4 \times 4$ unit cell nanowire. (b) Bandedge minima of the first four conduction subbands plotted along length of the nanowire in local bandstructure and VCA formulations. (c) Bandedge minimum in the transport direction plotted along length of the nanowire.

The Magnetic field is introduced into the tight binding Hamiltonian through Peierls substitution [27][28][29]. x' confinement resulting from the magnetic field is incorporated through the Landau gauge ($\vec{A} = Bx\hat{y}$). Closed boundary conditions are used in x and z directions while y -direction is assumed to be (quasi-)periodic. The confinement induced by closed boundary conditions in x' direction compete with the magnetic field confinement. The lateral extension of the strain and the electronic structure domain is set to 150nm, which is about 7 times larger than the maximum magnetic confinement

length in a 2DEG at $B = 1.5\text{T}$ ($\square 21\text{nm}$). For the magnetic field ranges of 1.5-4T confinement is dominated by the magnetic field and no lateral x-confinement effects due to the closed boundary conditions are visible in simulations of Figure 12. Modulation doping in Si/SiGe heterostructures induces built-in electric field. In the simulations performed here an electric field of 9 MV/m is assumed in the growth direction. SiGe alloy disorder is assumed to be quasi-periodic with the period of 5.5 nm which is sufficient to capture the effect of inhomogeneous strain disorder.

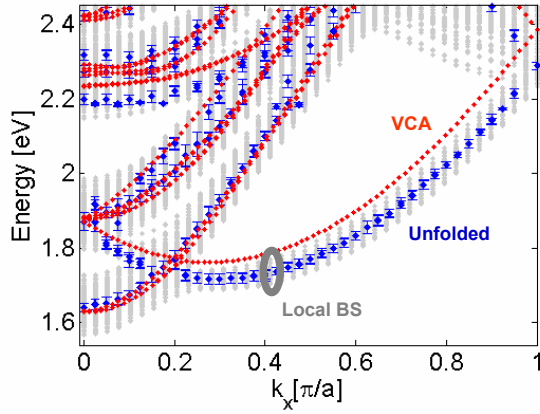


Fig. 14. Bandstructures of $40 \times 4 \times 4$ $\text{Si}_{0.8}\text{Ge}_{0.2}$ alloy nanowire in local bandstructure (grey), VCA (red) and zone-unfolding (blue) formulations.

In the presence of the applied magnetic field the 2-DEG is quantized in Landau levels (LLs). The valley-degeneracy of LLs is broken in the presence of sharp confinement due to Si/SiGe interfaces in a QW. The VS of first LL in flat and 2° miscut QWs is plotted as a function of the applied magnetic field in fig 16. The VS in ideal (no SiGe disorder) miscut QWs is 2 orders of magnitude less than that in flat QWs. The SiGe alloy disorder provides additional symmetry breaking leading to enhancement in VS in flat as well as miscut QWs (Figure 12). Addition of SiGe buffers to the electronic structure calculation domain in 2° miscut QWs results in VS close to the experimentally observed values.

Previous predictions of VS [24][25] over-predict the value of the VS compared to experimental data [26] while perfect slanted quantum wells underpredict the observed VS by an order of magnitude. Friesen et al [30] suggest that disorder in the miscuts raises the valley splitting to experimentally observed levels. Here we show that just buffer disorder with regular miscut steps alone can account for the additional valley splitting. We do not have to assume any particular step disorder models at all [31]. The atomistic representation of the confinement buffer and the local disorder in it is therefore an essential ingredient in the physics based simulation of VS. No additional disorder parameters need to be introduced to obtain results close to experiments! Simulations including step

roughness disorder combined with alloy disorder have recently been shown [31] to improve the agreement with experiment.

(D) SiGe Nanowires

Nanowires conduct carriers in one dimension and confine them in the other two dimensions. As the wire diameter is reduced to the nanometer range, it is understood that the two-dimensional confinement modifies the electronic structure and the nanowire is quite similar to an electromagnetic waveguide. Typical calculations are performed in the single band effective mass calculation. Full 3-D transport simulations based on NEGF have been implemented in simulators [13], analyzed interface roughness [32], and released on the nanoHUB [33]. Since its release in May 2006 the nanowire code has been used by over 419 users who have run over 3,898 simulations on a parallel virtual cluster utilizing VIOLIN [34] indicating that there is a real demand in the community for such simulations. It is however also understood that as the nanowire dimension shrinks to below around 5nm, that the effective mass approximation breaks down [35] and an atomistic representation of the material is needed to compute the dispersion of an ideal nanowire slice. Efforts are now underway to develop full 3-D nanowire NEGF-based transport simulators that are fully atomistic [15]. Fundamental questions to be addressed here remain the influence of the nanowire interface and the atomistic nanowire composition, such as alloy disorder.

Recently NEGF based transport simulations and full 3D electronic structure calculations were compared for AlGaAs nanowires [16]. A critical finding of that work was that the alloy disorder strongly influences the dispersion along the wire direction. The considered AlGaAs wires are unstrained and “only” contain atom disorder while all atom positions are on a regular zincblende GaAs/AlAs lattice. This work presents for the first time electronic structure calculations for SiGe nanowires that contain strain, position, and atom disorder. Different nanowire cross sections with 4, 6, 8 unit cells, corresponding to 2.17, 3.26, 4.34nm with a common nanowire length of 40 unit cells, corresponding to 22 nm are considered. Strain and electronic structure calculations are performed on the whole nanowire in free standing configuration. In other words substrate is not taken into account.

Figure 13a depicts a sliver cut through the center of the $40 \times 4 \times 4$ sample indicating the atomistically resolved disorder of the wire. Only the central 5nm long portion of this 22nm long wire is shown for good atomistic resolution. It is obvious that there is no such thing as a repeated unit cell in that wire. Therefore the very concept of bandstructure, which is based on a (small) repeated cell in semiconductors is called into question [36]. The most typical approach to deal with alloy disorder is called virtual crystal approximation (VCA). The VCA averages the atomic potentials according to the atom concentrations and to smooth out the material. In that approach a bandstructure can be easily calculated in the repeated 4×4 unit cell.

In another approach one can consider a single sliver of the 4×4 building block, imagine that that cell is repeated infinitely and compute a bandstructure in it. This would in a sense represent the local bandstructure for each slice. With the fluctuations in the device, one would expect that the conduction band edge will fluctuate from slice to slice as indicated in Figure 17b. SiGe alloy disorder splits 4 four fold degenerate bands in a pure Si nanowire. The corresponding bandedge minima of these four bands in $40 \times 4 \times 4$ SiGe alloy nanowire are plotted along length of the nanowire in Figure 13b. The four bands are degenerate in the VCA formulation and the bandedge minimum of this band is also plotted in Figure 13b. Figure 13c shows the X point conduction band minimum along the wire length in local band structure and VCA formulation. Each slice has its own local bandstructure and its fluctuations in k -space are compared in Figure 14 against the VCA approach. This local bandstructure approach does not deliver a meaningful bandedge of the wire or a meaningful effective mass.

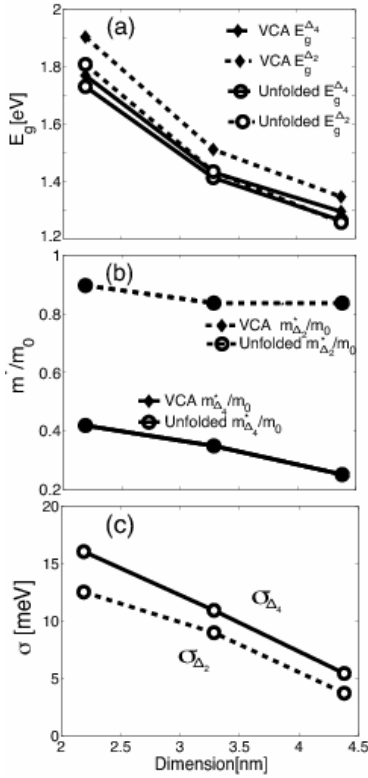


Fig. 15. (a) Direct (Δ_4 valleys) and indirect (Δ_2 valleys) bandgaps obtained from VCA and zone-unfolded bandstructures. (b) Effective masses of Δ_4 and Δ_2 valleys. (c) Energy uncertainties of Δ_4 and Δ_2 bands.

An alternative approach to the local bandstructure and the VCA approach is the computation of the electronic structure of the overall wire and to extract an approximate bandstructure that describes the overall wire well [36]. This approximate

bandstructure is representative of the overall transport capabilities of the wire and correlates well to NEGF transport simulations [16]. Figure 14 also compares the approximate bandstructure to the VCA and the local bandstructure samples. The approximate bandstructure provides a much more meaningful representation of the nanowire performance than the two others, which either over represent the disorder, or ignore disorder completely. From this approximate dispersions one can derive critical device parameters such as bandgap and effective masses (along the transport direction), which can be used in an approximate over-the-barrier-model to predict device performance [17][37].

Bandgaps and effective masses are plotted as a function of nanowire diameter in Figure 15a,b. The approximate bandstructure predicts a smaller bandgap than the VCA similar to AlGaAs nanowires [16] and AlGaAs bulk [38]. The direct (Δ_+) and indirect (Δ_-) valley-bandgaps show an interesting cross-over for 4.34nm wires, which will significantly increase the density of states at the conduction band edge and influence device performance; the VCA assumption does not result in such a cross-over. Interestingly the VCA and approximate bandstructure result in virtually identical effective masses. Additional statistical samples on different wires need to be simulated in the future to verify if this is a typical trend for this class of SiGe wires.

Since the bandstructure is approximate it does contain an error bar in energy for each k point in the dispersion. These energy uncertainties can be used to calculate the scattering time of the state according to the prescription of Ref [39]. One would expect that as the system becomes larger the error bars become smaller and the system becomes more bulk like. Figure 15c depicts the size of the error bars at the Δ_+ and Δ_- valley conduction band edges and indeed confirms that expectation. Note that even for the 4.34nm thick nanowire the fluctuations are still of the order of 5meV.

III. CONCLUSION

NEMO 3-D is introduced to the IEEE Nanoelectronics community as a versatile, open source electronic structure code that can handle device domains relevant for realistic devices. Realistic devices containing millions of atoms can be computed with reasonably, easily available cluster computers. NEMO 3-D employs a VFF Keating model for strain and the 20-band $sp^3d^5s^*$ empirical tight-binding model for the electronic structure computation. The impact of atomistic strain and piezoelectricity on the electronic structure in dome shaped quantum dots is explored. Under the assumptions of realistic boundary conditions, strain is found to be long-ranged and penetrate around 20 nm into the dot substrate thus stressing the need for using large dimensions of these surrounding layers and at least 3 million atoms in the simulations. The true symmetry of the quantum dots is found to be lower than the geometrical shape symmetry because of the fundamental atomistic nature of the underlying zincblende

crystal lattice. Atomistic strain is found to induce further optical polarization anisotropy favoring the [110] direction and pronounced non-degeneracy in the quantum dot excited states, magnitude (few meV) of which depends mainly on the dot size and surrounding material matrix. First order piezoelectric potential, on the other hand, favors the $[1\bar{1}0]$ direction, reduces the non-degeneracy in the P states and is found to be strong enough to *flip* the optical polarization in certain sized quantum dots. Simulations of QD stacks exemplify the complicated mechanical strain and quantum mechanical interactions on confined electronic states. Molecular states can be observed when the dots are in close proximity. Simulations of SiGe buffered Si QWs indicate the importance of band-to-band interactions that are naturally understood in the NEMO 3-D basis. VS is computed as a function of magnetic field matching experimental data. First simulations of disordered SiGe alloyed nanowires indicate the critical importance of the treatment of atomistic disorder. Typical approaches of a smoothed out material (VCA) or considerations of bandstructure in just individual slices clearly fail to represent the disordered nanowire physics.

NEMO 3-D demonstrates the capability to model a large variety of relevant, realistically sized nanoelectronic devices. It is released under an open source license and maintained by the NCN, an organization dedicated to develop and deploy advanced nanoelectronic modeling and simulation tools. NEMO 3-D is not limited to research computing alone; A first educational version including visualization capabilities has been released on nanoHUB.org and has been used by hundreds of users for thousands of simulations.

ACKNOWLEDGMENT

Supported by the Indiana 21st Century Fund, Army Research Office, Office of Naval Research, Semiconductor Research Corporation, and National Science Foundation under Grant No. EEC-0228390. The work described in this publication was carried out in part at the Jet Propulsion Laboratory, California Institute of Technology under a contract with the National Aeronautics and Space Administration. The development of the NEMO 3-D tool involved a large number of individuals at JPL and Purdue, whose work has been cited. Drs. R. Chris Bowen, Fabiano Oyafuso, and Seungwon Lee were key contributors in this large effort at JPL. Discussions with Andrei Schliwa is acknowledged.

REFERENCES

- [1] P.M. Petroff, *Single Quantum Dots: Fundamentals, Applications, and New Concepts*, Peter Michler, Ed., Springer, Berlin, 2003.
- [2] P. Michler, A. Kiraz, C. Becher, W. V. Schoenfeld, P. M. Petroff, Lidong Zhang, E. Hu, A. Imamolu, "A Quantum Dot Single-Photon Turnstile Device", *Science*, vol. 290, pp. 2282-2285, 2000.
- [3] E. Moreau, I. Robert, L. Manin, V. Thierry-Mieg, JM Gérard, and I. Abram, "Quantum Cascade of Photons in Semiconductor Quantum Dots" *Phys. Rev. Lett.*, pp. 87, 183601, 2001.
- [4] M. A. Reed, J. N. Randall, R. J. Aggarwal, R. J. Matyi, T. M. Moore, and A. E. Wetsel, "Observation of discrete electronic states in a zero-dimensional semiconductor nanostructure", *Phys. Rev. Lett.* 60, 535, 1988.
- [5] M. A. Reed, Quantum Dots, "Quantum Dots", *Scientific American*, vol. 268, no. 1, p.118, 1993.
- [6] Arakawa, Y., and Sasaki, H., "Multidimensional quantum well laser and temperature dependence of its threshold current", *Appl. Phys. Lett.*, 40, 939 (1982).
- [7] S. Fafard, K. Hinzer, S. Raymond, M. Dion, J. McCaffrey, Y. Feng, S. Charbonneau, "Red-Emitting Semiconductor Quantum Dot Lasers", *Science*, 22, 1350, 1996.
- [8] M.V. Maximov, Y.M. Shernyakov, A.F. Tsatsul'nikov, A.V. Lunev, A.V. Sakharov, V.M. Ustinov, A.Y. Egorov, A.E. Zhukov, A.R. Kovsch, P.S. Kop'ev, L.V. Asryan, Z.I. Alferov, N.N. Ledentsov, D. Bimberg, A.O. Kosogov, and P. Werner, "High-power continuous-wave operation of a InGaAs/AlGaAs quantum dot laser", *J. Appl. Phys.*, 83, 5561, 1998.
- [9] B. E. Kane, "A Silicon-based Nuclear Spin Quantum Computer", *Nature* 393, 133 (1998).
- [10] Pochung Chen, C. Piermarocchi, and L.J. Sham, "Control of Exciton Dynamics in Nanodots for Quantum Operations", *Phys. Rev. Letters*, 87, 067401 (2001).
- [11] Muhammad Usman, Shaikh Ahmed, Marek Korkusinski, Clemens Heitzinger, and Gerhard Klimeck, "Strain and electronic structure interactions in realistically scaled quantum dot stacks", *proceedings of the 28th International Conference on the Physics of Semiconductors*, ICPS 2006, Vienna, Austria, July 24-28 2006.
- [12] Gerhard Klimeck, Timothy Boykin, Mathieu Luisier, Neerav Kharche, Andreas Schenk, "A Study of alloyed nanowires from two perspectives: approximate dispersion diagrams and transmission coefficients", *proceedings of the 28th International Conference on the Physics of Semiconductors*, ICPS 2006, Vienna, Austria, July 24-28 2006.
- [13] J Wang, A Rahman, A Ghosh, G Klimeck, M Lundstrom, "Performance evaluation of ballistic silicon nanowire transistors with atomic-basis dispersion relations", *Applied Physics Letters* 86, 093113 (2005).
- [14] Y Zheng, C Rivas, R Lake, K Alam, TB Boykin, G Klimeck, "Electronic properties of Silicon nanowires", *IEEE Tran. Elec. Dev.*, Vol. 52, No. 6, June 2005 and references therein.
- [15] Mathieu Luisier, Andreas Schenk, and Wolfgang Fichtner, Gerhard Klimeck, "Atomistic simulation of nanowires in the $sp^3d^5s^*$ tight-binding formalism: From boundary conditions to strain calculations", *Phys. Rev. B*, 74, 205323, 2006.
- [16] Timothy B. Boykin, Mathieu Luisier, Andreas Schenk, Neerav Kharche, and Gerhard Klimeck, "The electronic structure and transmission characteristics of disordered AlGaAs nanowires," *IEEE Trans Nanotechnology*, 6, 43, 2007.
- [17] Anisur Rahman, Gerhard Klimeck, and Mark Lundstrom, "Novel channel materials for ballistic nanoscale MOSFETs bandstructure effects", *2005 IEEE International Electron Devices Meeting*, Washington, DC, December 5 - 7, 2005.
- [18] Marta Prada, Neerav Kharche, Gerhard Klimeck, "Electronic Structure of Si/InAs Composite Channels", Accepted as oral presentation in *MRS Spring conference 2007*, Symposium G: Extending Moore's Law with Advanced Channel Materials.
- [19] M. A. Eriksson, M. Friesen, S. N. Coppersmith, R. Joynt, L. J. Klein, K. Slinker, C. Tahan, P. M. Mooney, J. O. Chu, and S. J. Koester, "Spin-based quantum dot quantum computing in Silicon", *Quantum Information Processing*, 3, 133 (2004).
- [20] Gabriel Bester and Alex Zunger, "Cylindrically shaped zinc-blende semiconductor quantum dots do not have cylindrical symmetry: Atomistic symmetry, atomic relaxation, and piezoelectric effects", *Physical Review B*, vol. 71, 045318, 2005. Also, please see references therein.
- [21] Seungwon Lee, Olga L. Lazarenkova, Fabiano Oyafuso, Paul von Allmen, and Gerhard Klimeck, "Effect of wetting layers on the strain and electronic structure of InAs self-assembled quantum dots", *Phys. Rev. B*. Vol. 70, pg. 125307, 2004.
- [22] Seungwon Lee, Fabiano Oyafuso, Paul von Allmen, and Gerhard Klimeck, "Boundary conditions for the electronic structure of finite-extent, embedded semiconductor nanostructures with empirical tight-binding model", *Phys. Rev. B* 69, 045316, 2004.
- [23] Gabriel Bester, Xifan Wu, David Vanderbilt, and Alex Zunger, "Importance of Second-Order Piezoelectric Effects in Zinc-Blende Semiconductors", *Phys. Rev. Lett.*, vol. 96, 187602, 2006.

- [24] Timothy B. Boykin, Gerhard Klimeck, Mark Eriksson, Mark Friesen, S. N. Coppersmith, Paul von Allmen, Fabiano Oyafuso, and Seungwon Lee, "Valley splitting in strained silicon quantum wells", *Applied Physics Letters*, vol. 84, pp. 115-117, 2004.
- [25] Timothy B. Boykin, Gerhard Klimeck, M. A. Eriksson, Mark Friesen, S. N. Coppersmith, Paul von Allmen, Fabiano Oyafuso, and Seungwon Lee, "Valley splitting in low-density quantum-confined heterostructures studied using tight-binding models", *Phys. Rev. B.*, vol. 70, 165325, 2004.
- [26] S. Goswami, M. Friesen, J. L. Truitt, C. Tahan, L. J. Klein, J. O. Chu, P. M. Mooney, D. van der Weide, S. N. Coppersmith, R. Joynt, M. A. Erikson, *cond-mat/0408389*; S. Goswami, K. A. Slinker, Mark Friesen, L. M. McGuire, J. L. Truitt, Charles Tahan, L. J. Klein, J. O. Chu, P. M. Mooney, D. W. van der Weide, Robert Joynt, S. N. Coppersmith, Mark A. Eriksson, *cond-mat/0611221*.
- [27] Timothy B. Boykin, P. Vogl, "Dielectric response of molecules in empirical tight-binding theory", *Phys. Rev. B*, vol. 65, 035202, 2001.
- [28] M. Graf and P. Vogl, "Electromagnetic fields and dielectric response in empirical tight-binding theory," *Phys. Rev. B*, 51, 4940, 1995.
- [29] Timothy B. Boykin, R. Chris Bowen, and Gerhard Klimeck, "Electromagnetic coupling and gauge invariance in the empirical tight-binding method," *Phys Rev B*, 63, 245314 2001.
- [30] M. Friesen, M. A. Eriksson and S. N. Coppersmith, "Magnetic field dependence of valley splitting in realistic Si/SiGe quantum wells", *Appl. Phys. Lett.*, 89, 202106, 2006.
- [31] Neerav Kharche, Marta Prada, Timothy B. Boykin, and Gerhard Klimeck, "Valley-splitting in strained Silicon quantum wells modeled with 2 degree miscuts, step disorder, and alloy disorder", *Applied Phys. Lett.* Vol. 90, 092109, 2007.
- [32] Jing Wang, Eric Polizzi, Avik Ghosh, Supriyo Datta, and Mark Lundstrom, "Theoretical investigation of surface roughness scattering in silicon nanowire transistors", *Appl. Phys. Lett.*, 87, 043101, 2005.
- [33] https://www.nanohub.org/simulation_tools/nanowire_tool_information.
- [34] P. Ruth and J. Rhee and D. Xu and R. Kennell and S. Goasguen, "Autonomic Live Adaptation of Virtual Computational Environments in a Multi-Domain Infrastructure", *IEEE International Conference on Autonomic Computing ICAC*, 2006.
- [35] Jing Wang, Anisur Rahman, Gerhard Klimeck and Mark Lundstrom, "Bandstructure and Orientation Effects in Si and Ge Nanowire FETs", *2005 IEEE International Electron Devices Meeting*, Washington, DC, December 5 - 7, 2005.
- [36] Timothy B. Boykin, Neerav Kharche, Gerhard Klimeck, and Marek Korkusinski, "Approximate bandstructures of semiconductor alloys from tight-binding supercell calculations," *J. Phys: Condensed Matter*, 19, 036203, 2007.
- [37] Jing Wang, Eric Polizzi, Mark Lundstrom, "A three-dimensional quantum simulation of silicon nanowire transistors with the effective-mass approximation", *Journal of Applied Physics*, 96(4), pp. 2192-2203, 2004.
- [38] Fabiano Oyafuso, Gerhard Klimeck, R. Chris Bowen, and Timothy B. Boykin, "Atomistic Electronic Structure Calculations of Unstrained Alloyed Systems Consisting of a Million Atoms", *Journal of Computational Electronics*, vol. 3, pp. 317-321, 2002.
- [39] Timothy B. Boykin, Neerav Kharche, and Gerhard Klimeck, "Evolution time and energy uncertainty", to appear in *European Journal of Physics*, 2007.